Acta Astronautica 215 (2024) 348–361

Contents lists available at ScienceDirect

Acta Astronautica

journal homepage: www.elsevier.com/locate/actaastro

BLISS: Interplanetary exploration with swarms of low-cost spacecraft

Alexander N. Alvara [a,b,*], Lydia Lee [a,c], Emmanuel Sin [b], Nathan Lambert [a,c], Andrew J. Westphal [d], Kristofer S.J. Pister [a,c]

[a] Berkeley Sensors and Actuator Center, Berkeley, CA, 94720, USA
[b] Mechanical Engineering Department, University of California, Berkeley, Berkeley, CA, 94720, USA
[c] Electrical Engineering and Computer Sciences Department, University of California, Berkeley, Berkeley, CA, 94720, USA
[d] Space Sciences Laboratory, 7 Gauss Way, Berkeley, CA, 94720, USA

A B S T R A C T

Leveraging advancements in micro-scale technology, we propose a fleet of autonomous, low-cost, small solar sails for interplanetary exploration. The Berkeley Low-cost Interplanetary Solar Sail (BLISS) project aims to utilize small-scale technologies to create a fleet of tiny interplanetary spacecraft for rapid, low-cost exploration of the inner solar system. This paper describes the hardware required to build a ~10 g spacecraft using a 1 m^2 solar sail steered by micro-electromechanical systems (MEMS) inchworm actuators. The trajectory control to a NEO, here 101955 Bennu, is detailed along with the low-level actuation control of the solar sail and the specifications of proposed onboard communication and computation. Two other applications are also shortly considered: sample return from dozens of Jupiter-family comets and cometary nuclei imaging. The paper concludes by discussing the fundamental scaling limits and future directions for steerable autonomous miniature solar sails with onboard custom computers and sensors.

1. Introduction

Recent improvements in low-cost private-sector access to space, driven in part by the CubeSat standard have created a wide range of exciting and useful spacecraft [1,2]. CubeSats units (U) generally have a 1 kg weight and are 1000 cm^3 stackable from 1 to 24U in general usage, with 3U being the most widely used (64 %) [3] for various proposed missions such as ionospheric sensing [4] asteroid close-proximity imaging [5], analysis of radiation effects on biological samples during deep space exploration [6], quantum communication [7], ice thaw mapping [8], and much more. Even with the cost saving employment of COTS costs associated with CubeSat development for specific mission uses usually ranges well above $10,000 USD and takes years to develop [3]. Planet Labs has shown that hundreds of spacecraft with a volume of 3 L have commercial use-cases, and that spacecraft designed and assembled with consumer electronics standards can survive in low earth orbit (LEO). Manchester et al. [9] have deployed an orbital swarm of more than one hundred ChipSats, spacecraft at the size scale of a system-on-chip (often designed in the same processes as consumer electronics) weighing only a few grams each. The Breakthrough Starshot Initiative hopes to show that similar spacecraft can go to the nearest stars and return image data [10]. While many works detail the use solar sails, the continued use of specialized equipment that remains expensive and massive contributes to a high moment of inertia restricting the possibility of high agility maneuver which remains a technological challenge. Indeed, other work has described a smaller and similarly capable concept for deploying the ubiquitous SmartDust [11] as a femtosatellite, ChipSat, propelled by SRP as described by Niccolai et al. [12] where the SmartDust femtosattelite is simulated as a sun-facing particle of orbital dust using an Electrochromic Coating System (ECS) for attitude control in various mission possibilities with onboard camera, solar cells, computation, antenna, and battery.

The primary motivation behind small-scale solar sails is that practical, 10–100 m^2 solar sail spacecraft remain difficult to build [13]. Solar sails can suffer from low torques which inhibit attitude control, further motivating the need for larger sail area-to-mass ratio [14]. Indeed, the need for higher speed maneuvers motivate the reduction of moments of inertia and reduction of length-to-width aspect ratio as small SRP forces act on solar sails [15]. Consequently [14,15] stand as some of the first conceptual work for small solar sails. The high cost of depositing such a sail outside the Hill Sphere of Earth is another limitation and the selection of Earth escape trajectories is also limited by sail mass loading in that most proposed trajectories require relatively fast maneuvers to maintain heading. At a sail mass loading of 10 g/m^2, leaving Earth orbit and transiting to near-Earth objects (NEOs) both require roughly less than a couple years [16,17]. Such a mass loading also allows for more agile maneuvers, as discussed in Section 5. Unfortunately, achieving

* Corresponding author. Berkeley Sensors and Actuator Center, Berkeley, CA, 94720, USA.
E-mail addresses: engineer_alvara@berkeley.edu (A.N. Alvara), lydia.lee@berkeley.edu (L. Lee), emansin@berkeley.edu (E. Sin), nol@berkeley.edu (N. Lambert), westphal@berkeley.edu (A.J. Westphal), ksjp@berkeley.edu (K.S.J. Pister).

https://doi.org/10.1016/j.actaastro.2023.11.027
Received 3 September 2023; Received in revised form 12 November 2023; Accepted 18 November 2023
Available online 23 November 2023

Nomeclature

The next list describes several symbols that will be later used within the body of the document

β	Lightness number
δ	Clock angle
α	Cone angle
λ	Wavelength of light
m_p	Payload mass
m_{ss}	Solar sail mass
m_{ss}^{φ}	Roll sail mass
A_{ss}	Solar sail area
r_{ss}	Solar sail radius
x_p	Payload center of gravity x-position in body centered frame, similarly for y and z
x_{ss}^{φ}	Roll sail x-position in body centered frame, similarly for y and z
x_{ss}	Solar sail center of gravity x-postion in body centered frame, similarly for y and z
l_y	Shroud/tether length
SRP	Solar Radiation Pressure
COTS	Components Off-The-Shelf
F_N	Normal-to-sail SRP force
F_h	Perpendicular component of SRP force
F_r	Radial component of SRP force
F_t	Tangential component of SRP force
G_{sc}	Solar flux
c	Speed of light in a vacuum
$\hbar$	Planck's constant

such a low mass loading is a severe challenge for conventional spacecraft. Even CubeSats, among the smallest of spacecraft, require hundreds of square meters of sail area to achieve a mass loading of 10 g/m^2. Missions like New Horizons and OSIRIS-REx had a dry mass of hundreds of kilograms and would require sail areas in the tens of thousands of square meters, the area of many football fields, to achieve the desired mass loading. Sails of this size require sophisticated deployment design, and the difficulty of developing low-mass sail-deployment hardware has played a role in their lack of use to date. Other such future missions, such as the Advanced Composite Solar Sail [18] could also provide information about the ability for low-thrust small spacecraft and solar sail technology in particular. Similarly, the Solar Cruser mission [19] is projected to stand as a prime example for solar sail technology demonstration for Lagrange point halo orbiting.

The mission goal for this work is to deploy 100s–1000s of low-cost small solar sail spacecraft to NEOs for imaging with the goal of identifying asteroids that might have prospect of being deterred from a earth impact trajectories and those with the capacity for harboring organics and life within our solar system. The low mass of consumer electronics enables a new class of spacecraft driven by solar radiation pressure. These new capabilities have the potential to dramatically lower cost and decrease mission duration for inner solar system reconnaissance and sample return. There are roughly 20,000 known NEOs, roughly 1000 of which are believed to be asteroids greater than 1 km in diameter. Only 10 of these NEOs have been visited by spacecraft.

This work proposes a design that is intermediate in size to the above described spacecraft: much smaller and less massive than a CubeSat, with greater steering capability as compared with ChipSats and propelled by a non-consumable propulsion source by using solar sails. The Berkeley Low-cost Interplanetary Solar Sail (BLISS) project is intended to demonstrate that cell phone technologies and other miniaturization via technological advancements enable unprecedented capabilities in space. The novelty of this work is in showing that a low-cost alternative to interplanetary space exploration is possible for image collection of 100s of near Earth asteroids (NEAs) and sample capture of cometary material at low relative speeds to enable capture of any organics, the latter of which has been a goal of spaceflight for many years with few moderate successes [20]. Detailed is a selected intercept trajectory to a well known NEA, 101955 Bennu, for comparison and an Earth escape maneuver from GEO to offer a conservative demonstration of the capabilities for BLISS missions.

Section 2 provides an overview description of the BLISS spacecraft and the components therein. Section 3 details the dynamics, SRP thrust considerations, and the MEMS control assumptions. Section 4 describes an overview of the mission profile, entailing the generalized assumptions. Section 5 details the low-level control algorithm and optimized intercept trajectory. Section 6 details communication with special attention to SPAD use and a numerical exemplar for the proposed mission. Section 7 discusses the computation possible with the COTS components. Section 8 offers considerations for radiation as it pertains to COTS, MEMS, and solar sail materials. Section 9 is the discussion and future work component with considerations for other possible missions for the BLISS system. Section 10 offers a summary conclusion of the BLISS system, mission capabilities, and stated claims.

2. Spacecraft design

The proposed components for the BLISS spacecraft are listed in Table 1 along with their masses and an illustration highlighting the components and their relative positions is shown in Fig. 1. None of the components listed have masses more than a few grams, and most, such as the battery and motors, are a small fraction of a gram.

With the core of the spacecraft weighing roughly grams and costing less than $1000 USD, there are not many options for propulsion with the same order of magnitude in size and cost. Traditional chemical propulsion does not scale well to small sizes due to surface to volume issues with heat loss and low propellant burn rates [21]. Electric thrusters such as ion engines and electrospray engines are very promising, but are still orders of magnitude too large [22]. Until some other technique can be reduced to a mass of grams, the best propulsion for a 10 g spacecraft is a solar sail. The fundamental limits to this scaling are discussed in Section 8.

2.1. Solar sail sizing and packaging

With this mass, a solar sail that is just over a meter in diameter is needed to accomplish a sail loading of 10 g/m^2. Aluminized CP1 thin film at 1.0 μm thickness, weighs <2.8 g/m^2, and yet is strong enough to be handled, cut, folded, and thermally bonded. A carbon fiber rod can be bent into a ring on the perimeter of the aluminized CP1 sail [23]. It is also sufficiently flexible to be bent into a multi-turn flattened disk, and

Table 1
List of component masses and power consumption/capacity.

Component	mass (g)	Power (W)
Aluminized CP1 Sail	<2.8	–
MEMS Motors + IMU	<0.3	0.003
Optical Tx/Rx	2	5
HOPG Radiator Fin	1	–
LiPo Battery (x2)	0.66	2
iPhone Camera	<1	0.5
VoCore2	2.4	1.5
Alta Solar Cells (x2)	4	6
Total	**<14.16**	

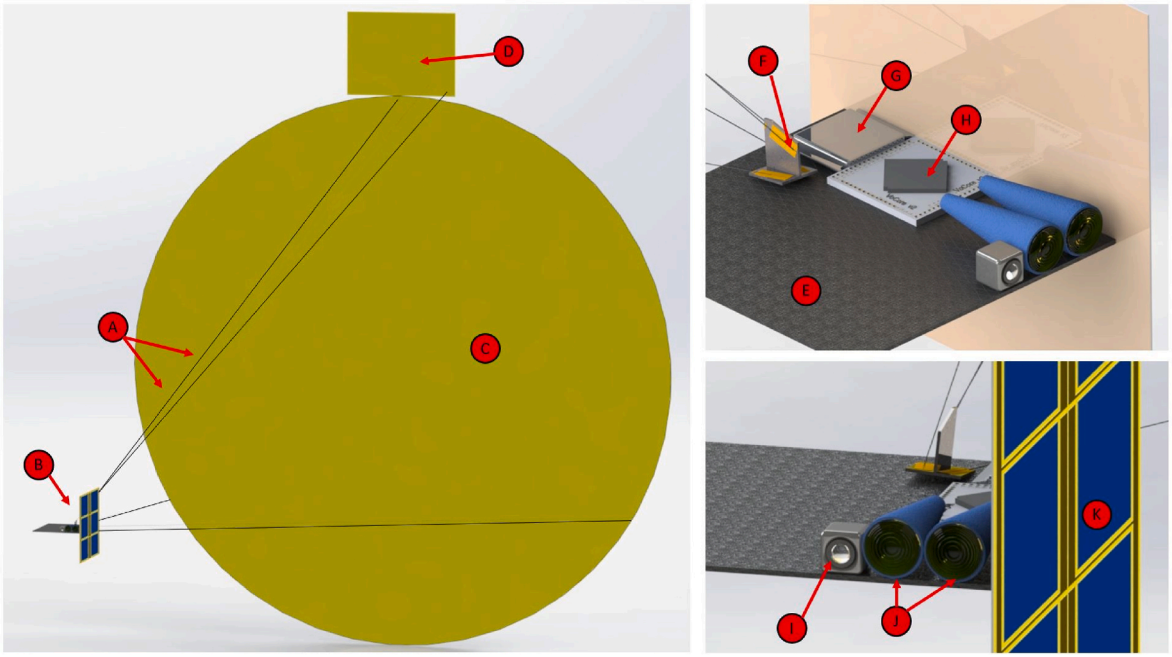

Fig. 1. Rendering of the BLISS spacecraft. Left: isometric view of the solar sail craft with A) carbon fiber rods, B) spacecraft body, C) CP1 main sail, and D) CP1 roll sail. Right-top:spacecraft body with E) HOPG radiator fin, F) MEMS motor actuators, G) LiPo battery, and H) VoCore2 CPU. Right-bottom spacecraft body with I) IPhone camera, J) optical 853 nm Tx/Rx, and K) solar panels.

sufficiently stiff to pop back to regular shape after release on orbit. Folds of three and five would allow a square meter sail to be carried inside a 9U or perhaps 3U CubeSat for early technology demonstrations [1,22]. In addition to the main sail, we will append a small sub-sail called the roll sail to one edge of the main sail to achieve control authority about all body axes. For a launch with one thousand spacecraft after the technology has been proven, the sails may be stored stacked on top of each other, with the spacecraft bodies arrayed around the perimeter. One thousand spacecraft of this type will weigh roughly 10 kg, and the stack of sails could be only a few millimeters thick.

2.2. Science payload

Imaging will be accomplished with a cell phone camera from within 1 km so that the asteroid fills the field of view (from an approximately 60° field of view angle the ideal distance away to fill the aperture is $\sqrt{3}r_{NEO}$). This will provide imaging with resolution on the order of 1–10 cm, enough to differentiate regolith or other surface types on asteroids.

Communication between a spacecraft and earth will be achieved by a semiconductor laser transmitter with a diffraction-limited 1 cm aperture, and a modestly sized single photon avalanche detector (SPAD) array with a receive aperture having a 10 cm diameter. This same hardware will allow peer-to-peer communication between spacecraft at more than one million kilometers, enabling a mesh network to pass data around the inner solar system. Digital processing and storage will consist of an off-the-shelf VoCore2 embedded LINUX computer running custom software. A micro-electromechanical system (MEMS) inertial measurement unit (IMU) will provide high-rate rotation sensing, and the CMOS camera will provide low-rate rotation sensing, star tracking, attitude determination, and rough localization. Propulsion will be provided by a roughly 1 m^2 solar sail, with MEMS motors controlling the sail and spacecraft orientation in 3 axes. Power will be provided by a 10 × 10 cm^2 primary solar panel, a small rechargeable lithium battery, and a few small solar cells distributed around the structure to maintain power during maneuvers. Thermal control will be accomplished by control of the orientation relative to the Sun of the primary solar cells, a small solar reflector, and a highly-oriented pyrolytic graphite (HOPG) radiator fin, in addition to management of the electronics power consumption.

3. Robot dynamics

In this section we detail the physical mechanisms that control the small solar sail through its spaceflight.

3.1. Thrust

Photons have energy E = hc/λ, and momentum p = h/λ = E/c. A flux of photons with power P being absorbed by a surface imparts a force equal to the change in momentum, $F_{photon} = P/c$. A perfectly reflective flat sail of area A at an angle α from the solar flux of $G_{sc} = 1.361$ kW/m^2 experiences a normal force of:

$$F_N = 2\frac{G_{sc}}{c}A\eta\, cos^2(\alpha) \approx \left(9\mu\frac{N}{m^2}\right)A\eta\, cos^2(\alpha) \tag{1}$$

This is the same as the gravitational attraction between the sail and the Sun at a distance of 1 AU if the mass loading of the sail is roughly 1.6 g/m^2. Real sails will have a reflection coefficient less than 1, some Lambertian reflection, and pressure from black body emission from the back side, making the peak normal force somewhat lower [24]. Here, η is taken from Ref. [25] to refer to the η-optical reflection model.

The radial (F_r), tangential (F_t), and normal (F_h), components of the force then become:

$$F_r = F_N\, cos(\alpha), \tag{2}$$

$$F_t = F_N\, sin(\alpha)\, sin(\delta), \tag{3}$$

$$F_h = F_N\, sin(\alpha)\, cos(\delta), \tag{4}$$

Taking δ to be $\frac{\pi}{2}$ it can be observed that the behavior in the plane of the ecliptic gives Ft = FN sin(α) and Fh = 0. The tangential force is maximized at an angle $sin^{-1}(1/\sqrt{3}) \approx 0.6$rad, giving a max tangential force of roughly $0.39F_N$. For near-circular orbits, this is the force that maximizes the rate of change of orbital energy. For a 10 g spacecraft with a 1 m^2 sail at 1 AU, this maximum force corresponds to an

acceleration of roughly 0.3 mm/s^2.

The sail force vector for an ideally reflective sail is always normal to the surface of a flat sail, and the radial component is always positive (away from the Sun). Nevertheless, a solar sail can still move toward the Sun by using the tangential force to slow its orbit [14]. For elliptical orbits, the desired force will vary in angle relative to the sun line. In general, the force in a particular direction relative to the Sun line is maximized by a sail cone angle of roughly one third of the desired angle [1].

While an ideal sail model is taken into account for this initial work, it should be noted that there are imperfections not considered; sail geometry such as wrinkling and billowing, sail material considerations such as optical uncertainties, temperature dependance, electrical dependance, and polymeric breakdown, as well as environmental considerations such as fluctuations in solar irradiance should be taken into account in a full mission profile. Here we provide an initial pass at the concept of utilization of low-cost solar sails with COTS. Many papers offer varied estimates on decrease in thrust and increase in uncertainty if thrust vector due to wrinkles and billowing [26,27]. However, when considering these works, it should be noted that most of the study on creasing, and to some degree wrinkling, of sails is attributed to the need to fold of large sails for encapsulation to fit within spacecraft prior to *in-situ* unfolding using extending structures. Also, much of the work on wrinkling and billowing is arranged around the need to have some hexagonal, rectangular, or triangular sail attached at a few points of fixation to a structural component [27]. In contrast, this work proposes a circular sail affixed at all points on the circumference which requires no such folding or creasing as it is made as-fabricated to be smaller than the transfer spacecraft containment inner diameter to reduce such effects, though it is noted that the effects will still be non-zero. Placing limitations on mission criteria could account for some issues arising due to optical irradiance and decrease of influence in SRP relative to solar wind by choosing to allot a reduced time of flight as well as selection of asteroids and comets to an outer limit of 0.5AU from the Sun and an inner limit of 0.1AU towards the Sun from Earth orbit [28], respectively. Billowing itself will still be an issue to account for as an effective source of error and uncertainty and must also be taken into account.

3.2. Rotation and steering

Achieving the desired cone angle requires utilizing shifts in the center of mass (COM) relative to the SRP pointing vector creating a torque about the COM. The main sail and the roll sail will be connected to the spacecraft body with four carbon fiber rods, here labeled *a-d*, roughly 0.3 mm in diameter and 2 m long. The rods *a-c* will be connected at one end to the main sail with *a* designated as the stationary rod and attached at the opposing end to the main body structure. Rods *b* and *c* are attached at their opposing end to MEMS linear inchworm motors adjusting length to control the relative position and orientation of the main sail to the spacecraft main body. Rod d will control the roll sail's relative motion and is affixed at one to the roll sail and the other end to MEMS motors similar to the previous two driven rods, b and c. The MEMS motors will be placed on the spacecraft body, as seen in Fig. 1. A cartoon depicting the axis and relative positions of the main sail, roll sail, carbon fiber rods, and the spacecraft body can be seen in Fig. 2, not to scale.

Parallel and differential actuation of the first and second carbon fiber rods will move the main sail relative to the craft's payload, offsetting the COM from the SRP pointing vector providing a moment about the COM of the system, allowing control of rotation about x-axis (pitch) and about z-axis (yaw). A fourth rod, with the third motor, will control the roll sail to generate a moment about the y-axis (roll). Here, a decoupled rotation approach is chosen where the rotations about the x- and z-axes neglect the contribution of torque due to the roll flag in the calculations below.

Coordinating movement of the inchworm motors gives an input acting on the main body of the spacecraft as:

$$\vec{q} = [q_a \; q_b \; q_c \; q_\varphi] \tag{5}$$

where q_i represents a linear movement, caused by the MEMS inchworm motors. Here, q_φ is the movement of the carbon fiber rod attached to the roll sail which induces a change in orientation in the roll sail itself. On the other hand q_b and q_c represent the linear movement of rods b and c which induces a translational change on the payload relative to the center-line of the main solar sail. The axes for these translations are set in the body centered frame originating at the COM and through the center of the main sail face and the COM of the payload where the y-axis runs along the length of the spacecraft, the z-axis runs from the COM to the direction of the roll sail, and the x-axis is perpendicular in the right hand convention. These axes are shown in Fig. 2 though in the diagram they are not placed at the origin for ease of viewing and to reduce cluttering. Note, the sail positions (x_{ss}, y_{ss}, z_{ss}) and payload positions (x_p, y_p, z_p) are all functions of the inputs, $\vec{q}$. The notation is simplified to be distances in their relative direction from the COM and a translation matrix sits between them.

MEMS electrostatic inchworm motors have a step size that is typically designed to be on the order of 1 μm, with a speed on the order of 1 mm s^{-1} [29], and Teal et al. [30] have shown a range that has been demonstrated at nearly 8 cm. For this work, an actuation range of $\leq \pm$ 10 cm, a speed of 1 mm s^{-1}, and a step size of 2 μm is simulated but smaller actuation ranges or slower maximum speeds are not considered a limiting factor for any mission specific maneuvers. The inchworm motors are powered by capacitive gap-closing actuator (GCA) arrays and push a centrally aligned spine and pawl with high frequency, electrically induced steps [31]. Applied to the meter-scale shroud lines of the sail, this will generate an angular change in the sail center-line of roughly one microradian (0.2 arc seconds) per step. There may be significant low-frequency dynamics excited by an abrupt step, so caution in motor design is necessary to avoide non-linear effects and higher order modes of excitation.

In the body-centered frame the principal mass moments of inertia are:

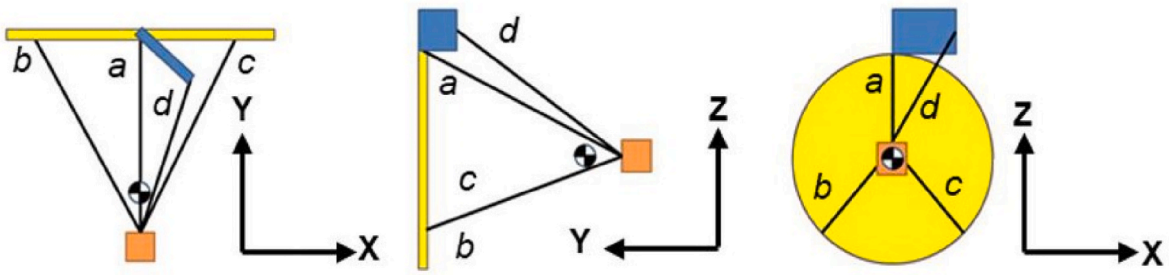

Fig. 2. Illustrating the BLISS body centered reference frame and approximate center of mass. Lengths not to scale. Left: x-y plane, Middle: y-z plane, and Right: z-x plane.

$$I_1 = \frac{1}{4} m_{ss} r_{ss}^2 + m_{ss}\left(y_{ss}^2 + z_{ss}^2\right) + I_{mp,xx} + m_p\left(y_p^2 + z_p^2\right) + m_{ss}^{\varphi}\left(x_{ss}^{\varphi\,2} + y_{ss}^{\varphi\,2}\right) \tag{6}$$

$$I_2 = \frac{1}{2} m_{ss} r_{ss}^2 + m_{ss}\left(x_{ss}^2 + z_{ss}^2\right) + I_{mp,yy} + m_p\left(x_p^2 + z_p^2\right) + m_{ss}^{\varphi} r_{ss}^{\varphi\,2} \tag{7}$$

$$I_3 = \frac{1}{4} m_{ss} r_{ss}^2 + m_{ss}\left(y_{ss}^2 + z_{ss}^2\right) + I_{mp,zz} + m_p\left(y_p^2 + x_p^2\right) + m_{ss}^{\varphi}\left(x_{ss}^{\varphi\,2} + y_{ss}^{\varphi\,2}\right) + I_{\varphi,zz} \tag{8}$$

where $I_{mp,xx}$, $I_{mp,yy}$, and $I_{mp,zz}$ are the inertial moment of mass for the spacecraft body COM used to indicate positions of components within the spacecraft as related to the parallel axis theorem in the $\hat{x}$, $\hat{y}$, and $\hat{z}$ body-centered coordinate system. Other cross terms exist and are negligible. For early experiments these represent the principal moments of inertia used in Section 5.1.

If the sail normal is moved about 1 mm from the COM in the x^-direction, the resulting pitch or yaw moment will be a torque of around 60 nNm, and an angular acceleration of:

$$\ddot{\alpha} = \frac{\tau_z}{I_{zz}} = \frac{F_N x_{ss}}{I_{zz}} \tag{9}$$

roughly 10^{-6} rad/s^2 if we take into account only the main sail giving a rough estimate for $I_{zz} \approx I_3$. Note, due to the symmetry shown in Equation (6), Equation (8), and Fig. 2 the rotation about the $\hat{z}$-axis behaves similarly to the rotation about the $\hat{x}$-axis. Rotations about the $\hat{y}$-axis are substantially slower due to lower peak torque from the smaller roll sail, but motions in this axis are primarily for thermal regulation and data collection. These present a much smaller set of problems with much longer timescales of motion than when compared to maneuvers needed to escape Earth's gravitational radius of influence (ROI).

The MEMS inchworm motors themselves maintain a consistent and predictable step size of 4 μm/step with interlocking pawls that engage at 2 μm intervals. These interlocks have a low but non-zero likelihood of slip and mis-step which can be taken to be a half interval, or 1 μm of mis-step in a given maneuver. This propagates to roughly 2 μm of offset in displacement in a given direction depending on which starting and ending orientation the BLISS system requires. Assuming a nominal tether length of 2 m with the above characteristics of moment of inertia, a nominal beginning pointing error can be on the order of 1 μrad with a propagation through small maneuvers of nearly 10x and large swift maneuvers like the ± 70° switch having nearly 50x that, giving a maximum pointing error of 50 μrad as determined from the above mentioned control law. Additional considerations for thermal management should be taken into account as differentials in coefficient of thermal expansion could introduce stress into the carbon fiber tether attachments creating non-symmetrical actuation and downstream errors in pointing angle. The connections between the other components will all be affixed with thermally conductive adhesive with a known coefficient of thermal expansion which will account for any induced stresses. Furthermore, the sail material itself will experience an expansion that trends with pointing angle and duration of time in a given orientation which should be studied in future work before deployment.

4. Mission profile

The mission profile entails orientation following an en-mass launch, spiraling out from a radius equivalent to geosynchronous earth orbit (r_{GEO}), interplanetary trajectory optimization, NEO approach, imaging, and return to Earth orbit for data transmission. Assuming that the spacecraft will be released near GEO, atmospheric drag will be negligible, as any orbit with a perigee above roughly 800 km is high enough that the energy gained per orbit from the sail is greater than the energy lost due to atmospheric drag. The return to Earth orbit mirrors the procedure to the interplanetary object.

4.1. De-tumble and orient

After release from the launch vehicle, the spacecraft will need to kill any residual rotation imparted by release. Orientation control of the spacecraft is provided by MEMS inchworm motors pulling on shroud lines on the sail. For rotation rates above 1° s^{-1}, the on-board IMU will inform the control system's decisions. Low-cost MEMS gyros have thermal-noise-limited resolution and bias drift of a small fraction of a degree per second. Below that rate, the camera will be used in a time lapse exposure to find the axis of rotation and rotation rate. Once the rotation rate is sufficiently low, a standard "lost in space" algorithm will be run on the star images to accurately determine orientation [32]. If there is sufficiently low magnitude and duration of tumbling on release, the IMU itself may be able to provide fairly accurate initial orientation estimates. During this initial phase, communication between spacecraft and the launch vehicle will be possible to a distance of a few hundred meters using the integrated WiFi radio available in almost all embedded LINUX platforms.

4.2. Spiral out

Once oriented, the spacecraft will begin the process of increasing its orbital altitude until it crosses out of the Earth's sphere of influence, utilizing a trajectory in the Sun-Earth orbital plane. A rough estimate for escape time is given by Ref. [24]:

$$t_{escape} = \frac{2800}{\beta\sqrt{6371 + h}} \text{ days} \tag{10}$$

where h is the initial orbital altitude in km, and β is the sail lightness number, the ratio of the maximum light pressure acceleration to the solar gravitation, which to first order is independent of distance from the Sun. For a sail mass loading of 10 g/m^2, $\beta \approx 0.16$. Starting from r_{GEO} in the plane of the ecliptic this process takes about three months.

Imaging the Earth, moons, and stars provides the necessary position input for the attitude control system to calculate the necessary sail angle during this process. The chosen in-plane spiral-out trajectory is one adapted from McInnes [24], where α traverses from 0° to 90° monotonically with the mean anomaly (θ), switches relatively quickly from 90° to 90° at the 'top' of the orbit, and then proceeds monotonically sweeping from 90° to 0° throughout the course of each orbit Section 5. During this phase of the mission, the spacecraft can be in periodic communication with ground stations on Earth using its primary optical communication system.

Alternate routes of positioning include being ferried by piggy-back on an existing Earth escape mission to avoid main belt transit and impeding effects due to perturbation by the Moon, however as these missions are somewhat hard to come by relative to missions to GEO, the current spiral out approach is provided as an example for a lower cost mission option.

4.3. Localization and matching orbits

During transit to the wide variety of NEOs, the spacecraft may be in communication with many of its neighbors, and able to use a combination of triangulation and optical time-of-flight (TOF) to determine its location in the solar system. Round trip TOF with a 1 Mbps optical communication system can easily achieve range errors of less than a kilometer at distances of at least one million kilometers, and small fractions of that error are possible with specialized hardware development. Pointing accuracy in the communication system should provide angular position measurements of roughly 0.1 mrad, or 100 km lateral accuracy at 10^6 km range, with errors accumulating the more hops the spacecraft is from a known reference point. If a fleet of spacecraft leaves the range in which communication with Earth is possible, it may have a reasonably accurate picture of the relative position of each member of

the fleet (kilometers of error or less), but a very poor estimate of where the fleet is in the solar system (one hundred thousand kilometers).

For those spacecraft without communication to their neighbors, they will rely on triangulation using the location of the planets against the stellar background. Unmodified cell phone cameras are able to take pictures of stars down to visual magnitude 5 through Earth's atmosphere. With minimal effort the inner six planets can be located in these images with an accuracy of roughly one milliradian. This will allow a spacecraft to localize itself in interplanetary space to within a few hundred thousand kilometers at a single point in time using several photographs. With better image processing algorithms and fusion of sensor data taken over many days, it is likely that this accuracy will improve by at least one order of magnitude. In either case, once it is close to the target NEO the spacecraft will use its camera to do terminal guidance.

Asteroids of 1–2 km diameter have absolute magnitudes, H, in the range of 15–17. The apparent magnitude, m is given by,

$$m = H + 5\log\frac{d_{BS}d_{BO}}{(1AU)^2} - 2.5\log(\Phi(\gamma)) \tag{11}$$

Where d_{BO} is the distance between the body and observer, d_{BS} is the distance between the body and Sun, and d_{OS} is the distance between the observer and Sun. Here γ is the angle between the body-Sun and body-observer lines, expressed as

$$\cos(\gamma) = \frac{{d_{BO}}^2 + {d_{BS}}^2 - {d_{OS}}^2}{2d_{BO}d_{BS}} \tag{12}$$

and Φ(γ) is the phase integral which accounts for the reflected light and is a number between 0 and 1 given by the approximation in Whitmell [33]. At 0.01 AU distance from the spacecraft, a 1–2 km diameter asteroid 1 AU from the sun will have an apparent magnitude of 5–7. So the spacecraft should be able to get close enough to a large asteroid by navigating based on sightings of the planets to be able to see the asteroid with the camera.

4.4. NEO image and return

The mission objective of asteroid imaging requires a down-selection to decide on an asteroid for case study that can act as a representative example for the benefits of the BLISS system in operation. As such, selection will be narrowed to include only near-Earth asteroids with diameters of 1–2 km. There are roughly 400 asteroids of 1–2 km diameter in near-Earth orbits [34]. Of these, the 101955 Bennu asteroid is taken as a prime example of state-of-the-art asteroid rendezvous recently accomplished. Images will be taken of Bennu from a parking orbit of 1–3 km from the surface. After the spacecraft has determined that it has sufficient images of the NEO, it will begin the return trip to Earth, following inverse order outlined for the trajectories specified in this paper. After the return trip, BLISS will transmit its data down to receivers on Earth from GEO in the case of imaging or data transmission or it will be captured by a nearby space station, i.e. the ISS, and studied there for the case of cometary sample retrieval.

5. Control and planning

Control of a solar sail spacecraft is a well studied problem in the context of orbit [20] and optimal trajectory control [35,36]. In this section we detail the control laws deployed to utilize MEMS inchworm motors for low-level control planning towards NEO rendezvous.

5.1. Low-level control

The discrete steps of the MEMS inchworm motors provide precise, reliable actuation to 1 μm or a quarter-step in actuation of the control rods which determine the pointing vector of the BLISS spacecraft the accuracy of which is discussed in Section 3.2 and compared to imaging resolution in Section 6.3.1. There will be two separate low-level control systems to maintain the robot's orientation in space: a pitch and yaw controller actuating the main sail and a roll controller actuating the auxiliary sail. Differential application of the two main control rods induces a desired linear shift of the force vector relative to the COM causing a pitch, roll, and yaw rotation following proportional-derivative (PD) control. Defining a local state of the system, $\vec{s}$ as:

$$\vec{s} = [x \quad y \quad z \quad \varphi] \tag{13}$$

the low-level controller will follow the desired state command from the trajectory planner outlined in Section 5.3. The four-dimensional control input, defined in Section 3.2, controls the attitude of the spacecraft. Given error from a desired orientation e_i (e.g. $e_\alpha = \alpha_d - \alpha$), PD control is defined by

$$u_i = K_P e_i + K_D \dot{e}_i \tag{14}$$

$$\epsilon_{attitude} \geq \|e_a\| \tag{15}$$

Initial selection of the PD control parameters is accomplished using standard linear control theory methods to get K_P and K_D initial values for simulation for the trajectories discussed in Section 5.3 and then hand tuning is performed to get higher order accuracy.

5.2. Earth orbit maneuvers

The modified orbit rate steering law (MORSL) will be used to accomplish Earth escape, which is adapted from McInnes [24]. In the original McInnes orbit rate steering law (OgMORSL), described as an orbit in the plane of the ecliptic, the spacecraft cone angle follows monotonically the mean anomaly in a counterclockwise rotation about Earth starting at the 3 o'clock position in a 45° cone angle, where 12 o'clock is the direction of Earth orbit in the projected heliocentric coordinate system. At the 12 o'clock position, the spacecraft flips orientation, presumably negligibly, swiftly such that it is relatively instantaneous and thereafter continues its cone angle rotation again matching monotonically to mean anomaly. The crucial low-level control maneuver for a solar sail orbiting around Earth in the plane of the ecliptic is the rapid switch of orientation to maintain the required orientation of the reflective side of the sail facing the Sun, assuming the 3 o'clock position is directly in the Earth's shadow as the Sun will be at the 9 o'clock position. Ideally, upon reaching the apex of an orbit, an ideal solar sail must switch from a cone angle of +90° to −90° [24] as indicated in Fig. 3.

Given constraints on the angular acceleration of the spacecraft body outlined in Section 3.2 and the drop-off in force on a solar sail with the sine of the cone angle, as it reaches ± 90° will approach zero (see Fig. 4).

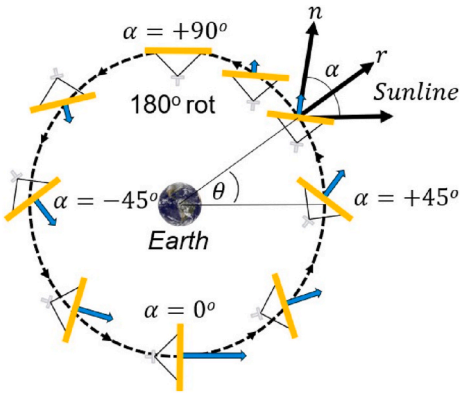

Fig. 3. McInnes orbit rate steering law showing direction of sail normal throughout a full circular orbit around Earth. Adapted from Ref. [24]. Not to scale.

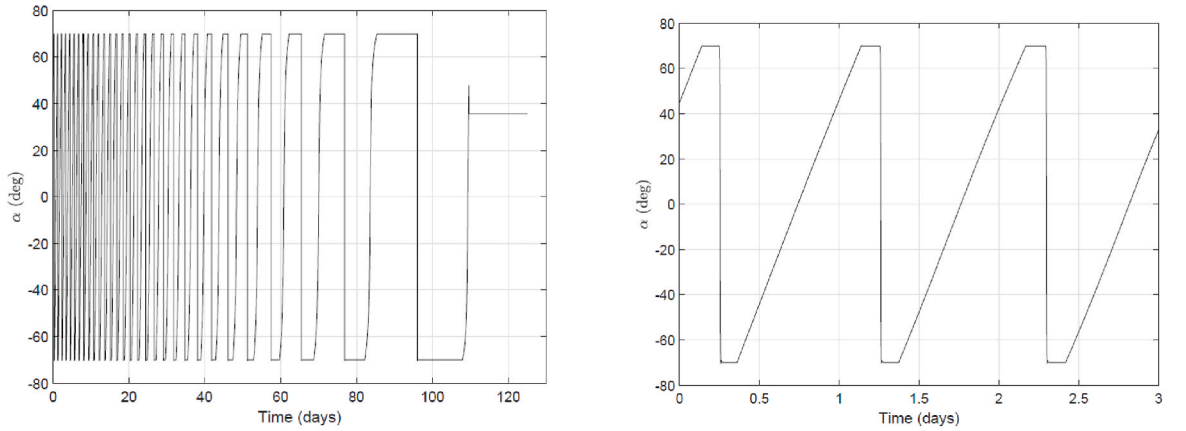

(a) Spiral out cone angle (125 days). (b) Spiral out cone angle (3 days).

Fig. 4. Simulated real cone angle for a) 125 days and b) 3 days.

As such, the cone angle is limited so as to maintain fine control of the trajectory. As the cone angle reaches 70° the SRP force nears 10 % of its nominal value and represents a chosen saturation limit. Additionally, the swift switch from $+70°$ to $-70°$ at the 'top' of the Earth orbit represents a crucial maneuver to managing orbital energy losses over the escape trajectory. These losses, if unchecked result in an overall slower orbit-raising trajectory, both increasing time to escape and also the likelihood of an undesirable early touchdown on the surface of the Earth as seen in Fig. 4a and 4b.

The downstream effect of inserting these practical non-idealities is an initially less rapid spiraling out of Earth orbit for the craft and a more eccentric orbit than the predicted OgMORSL which gains angular speed as the spacecraft spirals in towards the Earth on each successive orbit. Overall, this maneuver allows the spacecraft using the MORSL to trail the OgMORSL orbit by nearly 47 days, a relatively minor loss in performance that is overcome once leaving the Earth's gravitational pull Fig. 5. The MEMS motor steps can be seen throughout the earth escape maneuver in Fig. 6a and b. Table 2 shows the initial conditions of the trajectory and Fig. 7 shows the progression of the orbital parameters throughout the trajectory. Initial conditions are chosen using the conic-umbra approximation and chosen to be outside of the earth shadow for simplicity.

Future work will document the energy losses and other considerations when operating at different levels of Earth's orbit, including drag induced by diffuse particles of air in the upper exosphere, utilizing the tidal perturbations of the moon for a slingshot maneuver, singularities in the 3D case, trajectories utilizing Lissajous curves, and the effect of the Van Allen radiation belt on electrical and navigation performance including error correction operations.

5.3. Intercept trajectories

Here, treatment of the two-stage approach to the three-dimensional, near-Earth object (NEO) rendezvous problem is considered. In the first stage, the spacecraft matches the out-of-plane motion of the spacecraft, namely the inclination and longitude of the ascending node, to that of the NEO. A maximum inclination (and ascending node) rate-of-change steering law, as described in Ref. [24], may be used in this initial stage. Once the orbital plane change maneuver is complete, synchronization is accomplished to the in-plane motion in the second stage.

The following trajectory optimization problem is formulated to achieve in-plane rendezvous with the NEO. Since solar sails do not require fuel or energy to perform orbital maneuvers, a time-optimal objective Equation (16) is used, where the time of rendezvous, t_f, is a decision variable. Furthermore, be applying the assumption that the

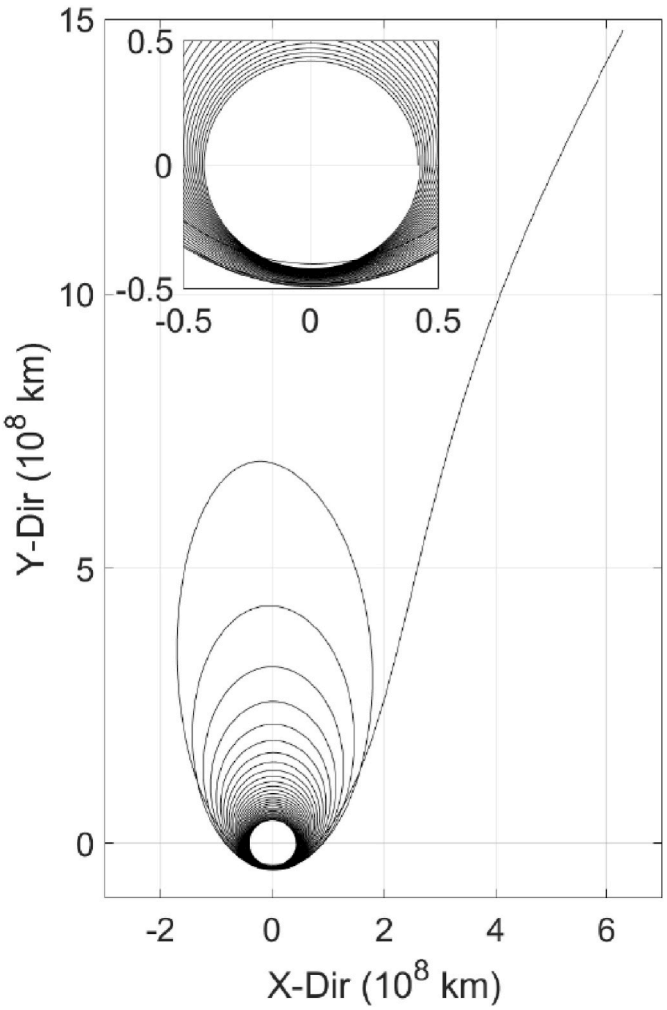

Fig. 5. Spiral out XY-trajectory. Inset showing close up around earth. Here X-Dir and Y-Dir are cartesian coordinates in the Earth-Moon frame.

collection of maneuver in the second-stage is entirely within the orbital plane, one may represent the spacecraft in this second-stage with a simpler four-state system expressed in a polar coordinate system Equation (17). The radial position r from the Sun's center, radial velocity u, and tangential velocity v may be normalized with respect to initial

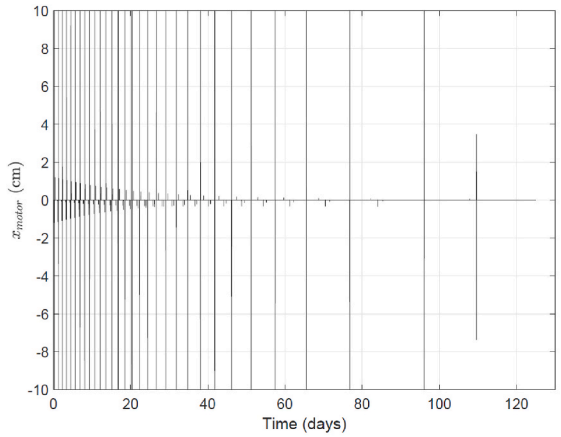

(a) Motor steps along 125 day trajectory.

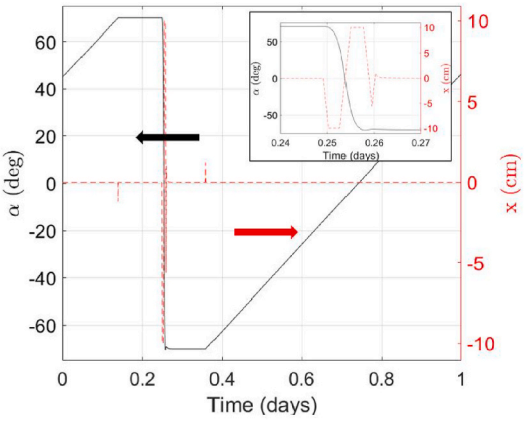

(b) Motor steps and cone angle along 1 day trajectory.

Fig. 6. a) Cone angle for the full trajectory and b) 1 day trajectory of cone angle (left y-axis) and motor steps of MEMS inchworm (right y-axis). Inset close up of first day of orbit showing motor steps during ± 70° switch maneuver.

Table 2
Initial conditions used for the Earth escape trajectory. Of note, IC for θ is non-zero due to starting outside of the earth-umbra, set by using the conic-umbra approximation and similarly $\dot{\theta}$, α, and $\dot{\alpha}$ are non-zero due to following of the embedded control law, MORSL, which ties the calculation of each to their angular and radial position about Earth in the Earth-Moon system.

ICs	Value	Units
α	0.8613	rad
$\dot{\alpha}$	3.6459×10^{-5}	rad/s
r	42164	km
$\dot{r}$	0.0000	km/s
θ	0.1516	rad
$\dot{\theta}$	7.2916×10^{-5}	rad/s

conditions Equation (18), and the angular position θ is with respect to a reference horizontal. Assuming a constant normalized peak solar sail specific force F for the spacecraft in the problem formulation. The rendezvous condition of matching positions is captured by Equation (19) where there is enforcement of the terminal Euclidean distance, expressed in Cartesian coordinates, between spacecraft and NEO to be within a tolerance value $\epsilon_{xy} = 10^{-5}$. The box constraints Equation (20) ensure that the rendezvous condition of matching velocities is satisfied with given tolerances, allowing the spacecraft to maintain the same orbital trajectory as that of the NEO. Note the assumed known state trajectory for the NEO in both polar and Cartesian coordinates, as represented by the overbar notation. Finally, control authority is derived from the cone angle α, the angle between the sail normal and the sun-sail line. The cone angle is bounded to be within $\pm 70°$ to avoid the loss of control authority at $\pm 90°$.

$$\underset{\alpha, t_f}{minimize} \int_{t_0}^{t_f} 1 \; dt \tag{16}$$

subject to

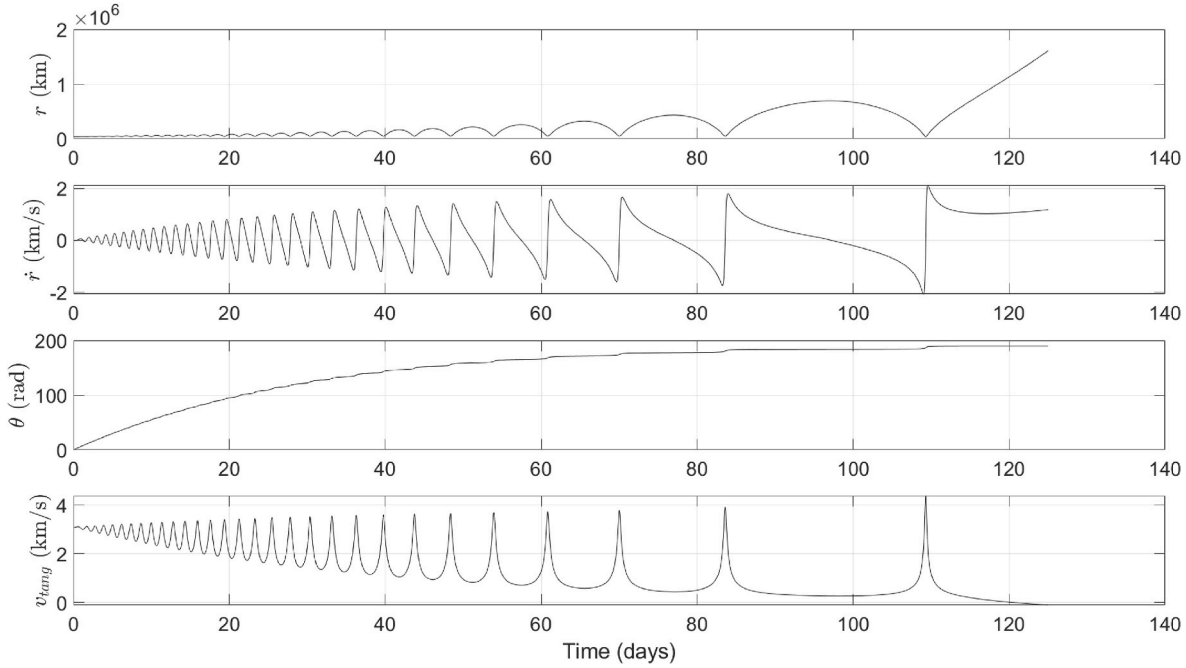

Fig. 7. Orbital parameters for Earth escape trajectory (125 days). Here r is radial distance from Earth in km, $\dot{r}$ is radial speed in km/s, v_{tang} is tangential speed in km/s, and θ is mean anomaly about Earth in degrees. The origin is set at Earth center and all coordinates are in the Earth-Moon frame.

$$\begin{bmatrix} \dot{r}(t) \\ \dot{u}(t) \\ \dot{v}(t) \\ \dot{\theta}(t) \end{bmatrix} = \begin{bmatrix} u(t) \\ \frac{v^2(t)}{r(t)} - \frac{1}{r^2(t)} + \frac{\widehat{F}}{r^2(t)} cos^3(\alpha(t)) \\ -\frac{u(t)v(t)}{r(t)} + \frac{\widehat{F}}{r^2(t)} cos^2(\alpha(t)) sin(\alpha(t)) \\ \frac{v(t)}{r(t)} \end{bmatrix} \quad \forall\, t \in [t_0, t_f] \tag{17}$$

$$[r(t_0) \quad u(t_0) \quad v(t_0) \quad \theta(t_0)]^\top = [r_0\ u_0\ v_0\ \theta_0]^\top \tag{18}$$

$$\left\| \begin{bmatrix} r(t_f)\cos(\theta(t_f)) - \bar{x}_{NEO}(t_f) \\ r(t_f)\sin(\theta(t_f)) - \bar{y}_{NEO}(t_f) \end{bmatrix} \right\|_2 \leq \epsilon_{xy} \tag{19}$$

$$\left| \begin{bmatrix} r(t_f) \\ u(t_f) \\ v(t_f) \end{bmatrix} - \begin{bmatrix} \bar{r}_{NEO}(t_f) \\ \bar{u}_{NEO}(t_f) \\ \bar{v}_{NEO}(t_f) \end{bmatrix} \right| \leq \begin{bmatrix} \epsilon_r \\ \epsilon_u \\ \epsilon_v \end{bmatrix} \tag{20}$$

$$|\alpha(t)| \leq \alpha_{max} \quad \forall\, t \in [t_0, t_f] \tag{21}$$

This problem formulation with nonlinear dynamics and non-convex constraints is solved using recent advances in sequential convex programming [37]. Although a single approach that simultaneously matches out-of-plane and in-plane motion may result in more time-optimal solutions, here it is illustrated that the problem may be separated into two trajectories providing a conservative rather than an optimistic time to objective for the given NEO. Future work will focus on a unified, single-stage approach to the rendezvous problem.

This numerical example uses the problem parameters listed in Table 3, where μ is the standard gravitational parameter of the Sun and r_0 is a reference distance. At this reference distance a specific value is assumed for the maximum solar radiation pressure, P. Assuming a spacecraft mass, m, and solar sail reference area, A_{ss}, the computed normalized peak solar sail specific force is $\widehat{F} = \frac{PA_{ss}}{m(\mu/r_0)^2}$.

The initial conditions of the solar sail and NEO are listed in Table 4, where the orbital positions and velocities of Earth and asteroid 101955 Bennu are assumed (projected on the Earth's ecliptic plane) at the epoch of September 8, 2016. In this preliminary study, it is assumed that the solar sail starts in the Earth's nearly circular orbit about the Sun where $\widehat{e}_1$ and $\widehat{e}_2$ are the primary and secondary Cartesian directions in the Earth's eliptical plane, these coordinates are different from X-Dir and Y-Dir which are in the Earth frame of reference.

As shown in Fig. 8a, our trajectory optimization problem finds a solution where the solar sail (solid, black trajectory) successfully completes a rendezvous with the NEO (dashed, red trajectory). Note that the solar sail's minimum-time strategy is to push radially outward, slowing down in speed, before returning towards the periapsis of its now highly elliptical orbit. Rather than attempting to "catch up" and close the angular displacement between the solar sail and the NEO, the solar sail effectively waits for the much faster NEO to complete a full orbit before rendezvous.

In Fig. 8b, it is observed that the optimal radial position and velocity of the solar sail match closely to those of the NEO at the end of the trajectory, signifying rendezvous. The duration of the maneuver is approximately 640 days (1.75 years), which compares with the 816 days for OSIRIS-REx's rendezvous with Bennu (launched on September 8, 2016 and rendezvous on December 3, 2018) [38]. As shown in the last plot of Fig. 8b, the angular displacement between the solar sail and NEO increases to produce a phase difference of more than one orbit.

The optimal solar sail cone angle is shown in Fig. 8c, where it is noted that the magnitude of the cone angle never reaches the ± 70° bounds. During this portion of the trajectory, maneuvers are on the scale of less than tens of degrees per day which is much slower than the required earth-escape trajectory's required maneuver speed of tens of degrees per second meaning that the MEMS controlled system is not overtaxed in speed or accuracy following any necessary maneuver within this section of the trajectory. The corresponding errors in each maneuver are easily correctible within the time scales limitations placed on the trajectory and result in a errors in cone angle that are negligible and correctable with the current controls in place ($\epsilon_\alpha \leq 10^{-6}$). The solar sail is constantly maneuvering with respect to the direction of solar sail radiation. The optimal input for this nonlinear system does not follow the minimum-time, "bang-bang" structure found for systems affine in the control variable [39].

Table 3
Parameters used for the trajectory optimization to 101955 Bennu.

Parameter	Value	Units
μ	1.327×10^{20}	m^3/s^2
r_0	1.495×10^{11}	m
P	9.08×10^{-6}	N/m
m	0.01	kg
A_{ss}	1.0	m
$\widehat{F}$	0.1531	

Table 4
Initial conditions for trajectory to 101955 Bennu.

Body	$\widehat{e}_1$ (AU)	$\widehat{e}_2$ (AU)	v_1 (km/s)	v_2 (km/s)
NEO	0.0018	0.9027	−34.0904	2.1930
Sail	0.9744	−0.2543	7.0391	28.7254

6. Communication

Free space optical communication is a mature field whose utility for space-based communication is similarly well-established [40]. This section considers an ultra long-range satellite-to-satellite communication during the course of the mission, as well as a terrestrial link from geostationary orbit.

Space-to-Earth communication and inter-spacecraft communication will be conducted via steered semiconductor laser transmitters with single photon avalanche diodes (SPADs) as photodetectors in a photon-starved environment.

6.1. Single photon avalanche diodes

Single photon avalanche diodes (SPADs) are PN junctions reverse biased past their breakdown voltage which give a readily detectable current pulse when a photon absorbed in the depletion region triggers avalanche breakdown; these pulses do not require analog amplification before digitization and are treated as discrete events.

6.1.1. Sensitivity

Sensitivity is quantified by wavelength-dependent photon detection probability (PDP),

$$\text{PDP}(\lambda) = \text{P}(\text{avalanche}|\text{event}) \times \text{QE} \tag{22}$$

where P(avalanche|event) is the probability of an avalanche given an event—the absorption of a photocarrier—and QE is the SPAD's quantum efficiency.

Accounting for device fabrication, the photon detection efficiency (PDE) is the photon detection probability, multiplied by the fill factor of the SPAD.

6.1.2. Noise

Uncorrelated device noise is characterized by the average rate of events in the absence of photons–known as the dark count rate (DCR)–measured in counts per second (Hz). DCRs today are on the order of singles to hundreds of counts per second at room temperature, though

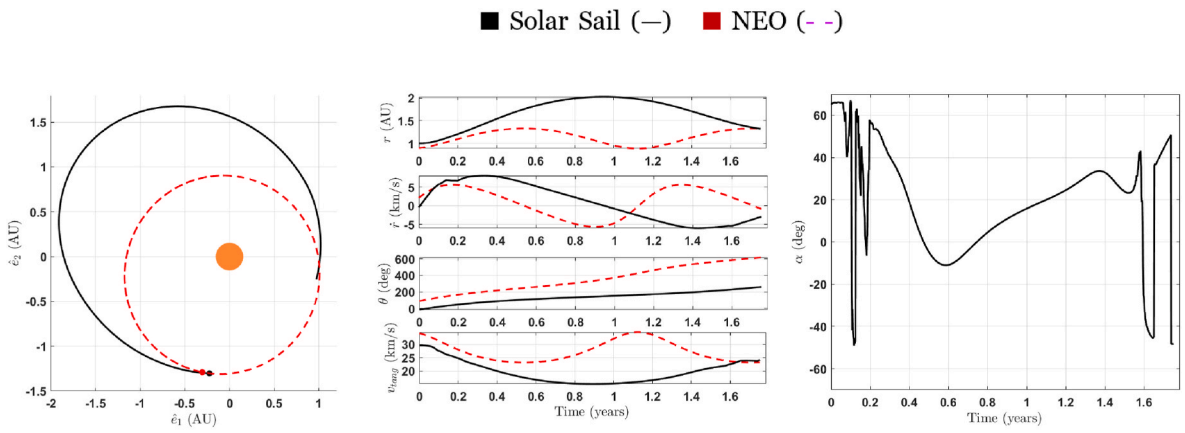

(a) Orbital trajectory to NEO (b) Orbital states for NEO intercept trajectory (c) Cone angle trajectory

Fig. 8. (a) Simulated, time-optimal trajectory of solar-sail to rendezvous with NEO about the Sun in the Earth elliptical plane where $\hat{e}_1$ and $\hat{e}_2$ are the primary and secondary Cartesian coordinates in the Sun-Earth orbital plane (Note: different from Fig. 5 X-Dir and Y-Dir which are in the Earth-Moon frame). The initial conditions of the planar problem are listed in Table 4. (b) The states for the time-optimal solar-sail and the NEO are r, radial position; $\dot{r}$, radial speed; v_{tang}, tangential speed; and θ, angle of the current position from start, set on September 8, 2016 all in the Sun-Earth orbital plane. (c) The optimal cone angle clearly operating within ±70° bounds to achieve NEO intercept using the in-orbital-plane trajectory.

exposure to high total doses of ionizing radiation increases both median DCR and its spread when measured across multiple SPADs [41,42]. Temperature dependence follows from its two primary mechanisms, with band-to-band tunneling dominating at low temperatures and trap-induced noise dominating at higher temperatures. Lower temperatures correspond to lower DCR at an exponential rate; while processing dictates the specifics of the exponential relationship [43], measured 20o ^{o}C per order of magnitude of DCR. Dead time is the interval after avalanche is triggered during which a SPAD can no longer detect incoming photons.

The self-sustaining nature of the SPAD's avalanche current necessitates a quenching circuit to stop the avalanche and reset the device to a detection-ready state. For megabit communication links, dead time approaching tens of nanoseconds—readily achievable with modern fabrication methods—is sufficient to avoid significant error due to dead time.

Afterpulsing occurs when carriers captured in traps during the initial photon-induced avalanche breakdown are released after the device has been quenched, triggering avalanche once more. Afterpulsing probabilities are often low enough (<0.1 %) to be negligible in overall analysis.

6.1.3. Arrayed receivers

While a single-SPAD receiver is appealing in its simplicity, dead time, device noise, and background light often make multi-SPAD arrays preferable to singular devices. One method of distinguishing signal photons from background and noise involves a minimum threshold on the number of counts to determine a digital HIGH.

For a random on-off keyed (OOK) bit sequence where P(0) = P(1) = 0.5, considering only uncorrelated noise the bit error rate is [44].

$$\mathrm{BER} = \left(\frac{1}{2}\sum_{i=n_T}^{\infty} p_Y^0(i)\right) + \left(\frac{1}{2}\sum_{i=0}^{n_T} p_Y^1(i)\right) \approx \left(\frac{1}{2}\sum_{i=n_T+1}^{\infty} N\left(i|\mu_0,\sigma_0^2\right)\right) + \left(\frac{1}{2}\sum_{i=0}^{n_T} N\left(i|\mu_1,\sigma_1^2\right)\right) \tag{23}$$

where n_T is the minimum number of counts required to constitute a 1, μ_0 is the average and σ_0^2 is the variance of the number of photons, N, detected during 0, and μ_1 and σ_1^2 are the same for 1.

While correlated noise such as optical crosstalk and afterpulsing affect BER, careful design can reduce their effect to the point of being negligible [45].

For OOK where DCR and afterpulsing are negligible, dead times approaching the bit time make it such that an array of SPADs can achieve the same BER as a single SPAD for fewer photons, i.e. lower optical power density at the receiver [46]. Although SPADs are fundamentally different from standard intensity-based photodetectors because of their dead time [46], also demonstrated a SPAD-based system capable of replacing traditional photodetectors in otherwise unchanged receivers.

6.2. Background light

This section will address sources of background light and methods to analytically determine photon counts for each.

Optical filtering is useful for limiting the number of undesirable background incident photons, though a non-normal incident angle of light θ_I shifts an interference-based filter's transmission peak, limiting the minimum feasible passlength for a given field of view. Equation (24) shows the shift in the filter's transmission peak from λ_0 as a function of shift in incident angle given an index of refraction n_{eff}.

$$\lambda_\theta = \lambda_0 \sqrt{1 - \left(\frac{n_0}{n_{eff}}\sin(\theta_I)\right)^2} \tag{24}$$

For example, for a YAG etalon optical filter with $n_{eff} = 1.8$ operating in free space with $\lambda_0 = 850$ nm, an off-normal angle of $\theta_I = 5°$ shifts the filter peak by 1.0 nm. In other words, to practically use a 2 nm filter of this type centered about λ_0 requires an angle of incidence no more than 5° off normal for the optical filter.

6.2.1. Point source

Stars in the receiver's field of view can be treated as point sources, with received power

$$P_{R,point} = \int A_R \eta_R \cdot H(\lambda) d\lambda \tag{25}$$

where A_R is the receiver aperture area, η_R is the receiving optics' efficiency, and $H(\lambda)$ is the spectral irradiance at the receiver.

Consider Vega, a commonly used A0Va reference star. Measured from the top of Earth's atmosphere 25 ly from the star, Vega's spectral irradiance peaks at roughly 8.5 × 10^{-11} W/(m^2 × nm) [47] at 400 nm. With a 10 nm optical filter centered about 400 nm, a 1 cm diameter detector receives approximately 66.7 fW, or 1.3 × 10^5 photons/s, from

the peak of Vega's spectral irradiance. Centering the optical filter about 850 nm yields 7.5 fW (3.2×10^4 photons/s). Vega is a magnitude 0 star; by magnitude 5 for the same stellar classification, the number of photons received decreases by two orders of magnitude.

6.2.2. Direct sunlight

Intuition suggests pointing a receiver directly at the sun poses an insurmountable obstacle for optical communication, but it is nonetheless useful to understand just how deleterious it is.

We begin with the spectral radiance of the sun B(λ) in the band of interest with Planck's Law, Equation (26), and convert from solid angle to area.

$$B(\lambda) = \frac{2hc^2}{\lambda^5} \frac{1}{e^{\frac{hc/\lambda}{k_B T}} - 1} \tag{26}$$

$$B_{sqm}(\lambda) = \int_0^{2\pi} \int_0^{\theta_{R,0}} B(\lambda) \sin\theta_R d\theta_R d\varphi = 2\pi B(\lambda)(1 - \cos\theta_{R,0}) \approx B(\lambda)\pi\theta_{R,0}^2 \tag{27}$$

where $\theta_{R,0}$ is the half angle of the sun as it appears from the receiver's position.

Using Equation (25), we calculate the optical power received due to direct sunlight,

$$P_{R,direct} = \int A_R \eta_R \cdot B_{sqm}(\lambda) d\lambda \tag{28}$$

At a distance 1 AU from the sun with a 1 cm diameter aperture and 100 % efficiency, operating with a 10 nm band-pass filter centered about 850 nm, we find $P_{R,direct} \approx 80$ μW, or 3.4×10^{14} photons/s at 850 nm.

Even at longer wavelengths with aggressive optical filtering and signal processing, direct sunlight precludes any direct detection schemes.

6.2.3. Indirect sunlight

Nearby objects in the receiver field of view will reflect light from a multitude of sources, most notably the sun. For an object with a reflectivity ρ a distance R away from the detector, and a detector angular subtense DAS, Equation (29) gives the received power due to indirect sunlight.

$$P_{R,indirect} = \int A_{obj} \cdot \rho \cdot \frac{A_R \eta_R}{\pi R^2} \cos\theta_{det} \cdot B_{sqm}(\lambda) d\lambda \tag{29}$$

where $A_{obj} = (R \cdot DAS)^2$ is the area projection of the detector onto the object and θ_{det} is the target angle relative to the detector.

We consider a system with the same lossless 1 cm diameter receiver as before, 1 AU away from the sun with a 10 nm filter centered about 850 nm.

The receiver is pointing directly at the reflecting object $\theta_{det} = 0$, the object is a perfect reflector $\rho = 1$, and the DAS is roughly λ/D_R rad with the diameter of the receiver aperture D_R. This DAS corresponds to the diffraction limit of the receiver optics.

The received power from indirect sunlight in this case amounts to roughly 1.8 pW, or 7.7×10^6 photons/s — many orders of magnitude lower than direct sunlight, but still likely large enough to overwhelm any direct detection scheme with a sufficiently reflective object, particularly if the reflector appears as more than a spot from the receiver point of view.

6.3. Alignment

Assuming aberration-free transmitting optics, the full-width half-maximum of the beam's power measured at the transmitting optics' focal plane is $1.028\lambda/D$, and the first null falls at $1.22\lambda/D$ from the center of the beam. The central beam is well approximated by a Gaussian with RMS width $\sigma \approx 0.42\lambda\frac{f}{d}$ where f is the focal length of the transmitting optics. An angular pointing error of $0.5\lambda/D$ rad at the transmitter corresponds to a halving of received power.

6.3.1. Numerical exemplar

Suppose we have a commercial edge emitting $P_T = 10$ W, $\lambda = 850$ nm laser with lossless optics providing a 1 cm diameter aperture with area A_T. With a lossless $\eta = 1$ receiver with a 1 cm diameter aperture area A_R stationed $R = 1.0 \times 10^9$ m from the receiver with no pointing error, the maximum optical power that can reach the receiver, Eq. (30), is 85.4 fW, or 3.7×10^5 photons/s.

$$P_R = P_T \frac{A_T A_R}{\lambda^2 R^2} \eta \tag{30}$$

With a 10 nm optical filter centered about 850 nm, we find (Table 5) that for a direct detection scheme, steps must be taken to avoid pointing the receiver directly at the sun or at highly reflective objects.

Care must be taken to avoid pointing at the sun, and strong reflectors can similarly complicate communication. Per Equation (23), pointing this system at a magnitude 5 A0Va star while avoiding direct and reflected sunlight, a 16-SPAD array with PDE approaching 0.6 can theoretically achieve 50 kbps downlink with a BER of 1×10^{-2} for 5 W average power consumed by the transmitting laser. Increasing the receiver aperture area by 10 × with otherwise identical hardware can attain up to 100 kbps downlink, corresponding to roughly 37 received signal photons per bit, with a BER approaching 1×10^{-3} with a transmitter pointing accuracy of roughly ±45 μrad, even with SPAD dead time on the order of singles of microseconds. Alternative modulation schemes and coherent detection can enable greater communication rates with still lower power, though adjustments from the classical analog regime to photon counting are necessary.

From GEO with atmospheric transmission $\eta \approx 0.5$ talking to an Earth-based receiver with a 10 cm aperture, the transmitter beam can have significantly greater divergence. A minuscule 500 μm transmit aperture can achieve data rates well in excess of 100 kbps with a pointing accuracy on the order of 1 mrad.

Per Equation (30), increasing the transmitter or receiver aperture permits inversely scaled transmitter power for the same performance. In other words, a commercially available 10 W NIR source, paired with transmit and receive apertures on the order of millimeters and tens of centimeters respectively can achieve data rates above 100 kbps with a bit error rate of 1×10^{-3} with a photon counting-based receiver.

7. Computation and storage

Cell phones and the internet of things have led to a wide range of choices in energy efficient, physically small computation platforms [48, 49]. The candidate platform should have the computational capabilities to store and process high resolution images. Other storage and processing requirements, such as guidance navigation and control, and communication processing, place significantly lower demands on processing and storage. Even the image processing task has relatively low requirements, with allowable processing times on the order of minutes or perhaps even hours.

Outperforming these requirements is available in a variety of single-board computers, of which the VoCore2 PC [50] is a representative. This $25 computer runs Linux on a 580 MHz MIPS 24K processor with 128

Table 5
Incident photons for a receiver with a 1 cm diameter aperture accompanied by a 10 nm filter centered about 850 nm. All values scale linearly with receiver aperture area.

Source	Photons/Second
Signal HIGH	3.7×10^5
Magnitude 5 A0Va	3.2×10^2
Direct Sunlight	3.4×10^{14}

MB of RAM and 16 MB of flash. The entire computer weighs 2.5 g, including connectors for camera and power, empty board space, and a microSD card slot. Adding a 512 GB card to store images and other data increases the system weight by roughly 0.25 g. The processor burns roughly 1W peak, and has many power control modes and has a temperature operating range from 0 °C to 85 °C.

Similar computational capability in a carefully designed board with commercial off-the-shelf components could weigh roughly a gram, and operate from 40 °C to 85 °C. Custom designed silicon would drop the mass to well under a gram and increase the allowed temperature range while allowing radiation hardening by design.

8. Radiation effects

Ionizing radiation in interplanetary space is a challenge for electronics. The BLISS mass budget does not allow for sufficient shielding to have a significant impact on the dose hitting the electronics. Still, carefully-designed electronics should be able to survive a multi-year mission with sufficient probability that a swarm of spacecraft will achieve useful mission results. Multiple measurements put the normal radiation dose at 0.1 to 0.2 Gy per annum [51–53]. Modern CMOS appears to be less susceptible to total ionizing dose than older technologies, perhaps due to gate oxides becoming so thin that trapped charges quickly tunnel away. Whatever the reason, it has been demonstrated that a 14 nm FINFET can survive at higher dosage levels. Hughes et al. [54] report leakage and threshold voltage shifts in several 14 nm FET technologies after exposure to various levels of total ionizing doses. Their conclusions are that the electronics can survive roughly 100 krad (1 kGy) without serious effect, and up to 1 Mrad (10 kGy) with careful circuit design. Surviving single-event upsets will require redundancy in both hardware and software through either additional COTS components or custom circuitry.

9. Discussion and technology trends

The capabilities showcased here highlight the potential for swarms of low-cost spacecraft in the 10s of grams weight range with a relatively small form factor for observation, and possibly sample return, available with COTS. The time to escape from near-Earth orbit was approximately 120 days, swinging out to 2 AU in under a year, completing the interplanetary travel to intercept Bennu at approximately 1.3 AU in 640 days, orbiting for 346 days to collect images (similar orbit time as Osiris-REx), and returning to earth-orbit in similar time to intercept brings round-trip mission time to completion in just over 5.1 years (1866 days) which is comparable to most small scale short missions but much faster than a similar Osiris-REx mission to an NEA which took just over 7 years (2572 days). Although the Osiris-REx mission to Bennu included a significant time to select a site for material retrieval and subsequent material gathering it is still a valuable benchmark for a case study such as this, especially when considering overall flight time. Future demonstration of the potential of the new small-scale spacecraft development will proceed in phases. The first science mission we propose will be to image 10s–100s of NEOs. The second will be to collect pristine cometary materials from 1000's of Jupiter-family comets. Missions to many celestial objects are within the capability of our 10 g robot, but for an initial demonstration, choosing targets with orbits close to 1 astronomical unit (AU) from the Sun simplifies the design of the power and thermal systems on the spacecraft.

For a spacecraft that returns to earth orbit to communicate, the ultimate limits to spacecraft size are perhaps an order of magnitude smaller than what is proposed here. All of the major systems (camera, computation and storage, communication, power) can be engineered for a mass of roughly 0.1 g each. For a spacecraft of total mass 1 g a sail of only 0.1 m^2 weighing only 0.1 g will suffice. This presents an opportunity in the field to gain an agile tool for observation capable of a broad scope of missions with a relatively quick turnaround. Bringing to the forefront the possibility of customized missions for each interested scientist, company, or otherwise interested party at a fraction of the current cost. Direct spectrography and microanalysis have long been the metric for understanding material composition. To that end, this work also proposes that the BLISS spacecraft can retrieve cometary samples for analysis on Earth. Comets in the inner solar system such as 107P Wilson-Harrington are a prime target for missions and the trajectory will be similar to that of the NEA rendezvous described earlier in this work.

In addition, any individual BLISS spacecraft can establish communication with its neighboring BLISS Linked Partner Spacecraft (BLiPS) to establish a network of intercommunication. Individual BLISS spacecraft can then utilize the BLiPS network to update navigation based on a voting system, increasing redundancy. BLiPS teams can also be used to capture multiple angles of a selected NEA or comet with fly-by maneuver (s) possibly allowing for a semi-3D reconstruction if some form of LIDAR is implemented in future iterations.

Beyond NEO reconnaissance, there are many potential applications of BLISS, and BliPS networks, in solar system exploration and planetary science. Swarms of approximately 10 g interplanetary spacecraft would enable rapid sample return from dozens of Jupiter-family comets. Comets contain the building blocks of the solar system, preserved in deep freeze for 4.6 billion years. Sample return of pristine cometary material was identified as a high priority in the most recent Planetary Decadal Survey, and a comet sample return mission — from a single comet — was one of two finalists in the most recent New Frontiers ($1B-class) competition. Even with an aggressive schedule, cometary samples would be expected no earlier than the mid-2040's with a New Frontiers approach. However, a fleet of 10 g interplanetary spacecraft has the potential to collect cometary samples from dozens of Jupiter-family comets within the next decade. Because cometary materials are complex on the submicron scale, large samples are not required for cometary sample return: the thousands of 10 μm rocks and abundant organic materials would keep the cosmochemistry community busy for decades.

10. Conclusion

This paper presents a vision for the Berkeley Low-cost Interplanetary Solar Sail spacecraft using microscale actuators and small solar sails to explore NEOs. The initial actuation, control, communication, and computation tools required to realize the BLISS project rely on the continued acceleration of spaceflight projects that reduce launch costs and the use of micro-technologies. The tools presented in this paper represent the initially available mechanisms, and with specific research the parameters for the spacecraft can be improved substantially, which would move the progress of the project towards first launch and allow exploration of more ambitious profiles for future missions. In providing a large base of results demonstrating the feasibility of such technologies, we hope that is opens further investigation into novel spacecraft and mission profiles.

Declaration of competing interest

The authors declare the following financial interests/personal relationships which may be considered as potential competing interests: All the authors (Alexander N. Alvara, Lydia Lee, Emmanuel Sin, Nathan Lambert, Andrew J. Westphal, and Kristofer S.J. Pister) all declare that they have no known competing interests, financial or otherwise that could have appeared to influence the work reported in this paper.

Acknowledgements

The authors would like to thank the Berkeley Sensor and Actuator Center (BSAC) for its continued support. This project was accomplished in part with funding from the National Science Foundation Graduate Research Fellowship Program (NSF-GRFP), the National GEM Fellowship, the Ford Predoctoral Fellowship, the Robert P. Lin SSL Fellowship,

and the Diversity & Community Fellowships. Also, thanks to Raymond Chong and Beau Kuhn for participating in many useful conversations.

References

[1] Jordi Puig-Suari, Clark Turner, William Ahlgren, Development of the standard cubesat deployer and a cubesat class picosatellite, in: 2001 IEEE Aerospace Conference Proceedings (Cat. No. 01TH8542), vol. 1, IEEE, 2001, pp. 1–347.

[2] Armen Poghosyan, Alessandro Golkar, Cubesat evolution: analyzing cubesat capabilities for conducting science missions, Prog. Aero. Sci. 88 (2017) 59–83.

[3] Thyrso Villela, Cesar A. Costa, Alessandra M. Brandão, Fernando T. Bueno, Leonardi Rodrigo, Towards the thousandth CubeSat: a statistical overview, Int. J. Aerospace Eng. 2019 (2019) 13, https://doi.org/10.1155/2019/5063145. Article ID 5063145.

[4] Cristiana Francisco, Ricardo Henriques, Susana Barbosa, A review on CubeSat missions for ionospheric science, Aerospace 10 (7) (2023) 622, https://doi.org/10.3390/aerospace10070622.

[5] Claudio Bottiglieri, Felice Piccolo, Carmine Giordano, Fabio Ferrari, Francesco Topputo, Applied trajectory design for CubeSat close-proximity operations around asteroids: the milani case, Aerospace 10 (5) (2023) 464, https://doi.org/10.3390/aerospace10050464.

[6] Sofia Massaro Tieze, Lauren C. Liddell, R. Sergio, Santa Maria, Sharmila Bhattacharya, BioSentinel: a biological CubeSat for deep space exploration, Astrobiology.Jun (2023) 631–636, https://doi.org/10.1089/ast.2019.2068.

[7] Luca Mazzarella, Christopher Lowe, David Lowndes, Siddarth Koduru Joshi, Steve Greenland, Doug McNeil, Cassandra Mercury, Malcolm Macdonald, John Rarity, Daniel Kuan Li Oi, QUARC: quantum research cubesat—a constellation for quantum communication, Cryptography 4 (1) (2020) 7, https://doi.org/10.3390/cryptography4010007.

[8] Lingcao Huang, Jing Luo, Zhanju Lin, Fujun Niu, Lin Liu, Using deep learning to map retrogressive thaw slumps in the Beiluhe region (Tibetan Plateau) from CubeSat images, Rem. Sens. Environ. 237 (2020) 111534, https://doi.org/10.1016/j.rse.2019.111534. ISSN 0034-4257.

[9] Zachary Manchester, Mason Peck, Andrew Filo, Kicksat: a crowd-funded mission to demonstrate the world's smallest spacecraft, in: 27th Annual AIAA/USU Conference on Small Satellites, August 2013. http://zacmanchester.github.io/docs/KickSat_SmallSat.pdf.

[10] Patricia Daukantas, Breakthrough starshot, Opt Photon. News 28 (5) (2017) 26–33.

[11] J.M. Kahn, R.H. Katz, K.S.J. Pister, Next Century Challenges: Mobile Networking for "Smart Dust" in Proceedings of the 5th Annual ACM/IEEE International Conference on Mobile Computing and Networking (MobiCom '99), Association for Computing Machinery, New York, NY, USA, 1999, pp. 271–278, https://doi.org/10.1145/313451.313558.

[12] Lorenzo Niccolai, Marco Bassetto, Alessandro A. Quarta, Giovanni Mengali, A review of Smart Dust architecture, dynamics, and mission applications, Prog. Aero. Sci. 106 (2019) 1–14, https://doi.org/10.1016/j.paerosci.2019.01.003. ISSN 0376-0421.

[13] Richard L. Garwin, Solar sailing-a practical method of propulsion within the solar system, Jet Propulsion 28 (3) (1958) 188–190.

[14] C. Jack, C.S. Welch, Solar kites: small solar sails with no moving parts, Acta Astronaut. 40 (2–8) (1997) 137–142.

[15] C. Jack, R. Wall, C.S. Welch, Spacefarer solar kites for solar system exploration, J. Br. Interplanet. Soc. (JBIS) 58 (5–6) (2005) 155–166.

[16] Lorenzo Niccolai, Alessandro A. Quarta, Giovanni Mengali, Analytical solution of the optimal steering law for non-ideal solar sail, Aero. Sci. Technol. 62 (2017) 11–18, https://doi.org/10.1016/j.ast.2016.11.031. ISSN 1270-9638.

[17] Andrea Caruso, Giovanni Mengali, Alessandro A. Quarta, Lorenzo Niccolai, Solar sail optimal control with solar irradiance fluctuations, Adv. Space Res. 67 (9) (2021) 2776–2783, https://doi.org/10.1016/j.asr.2020.05.037. ISSN 0273-1177.

[18] William K. Wilkie, Book Chapter. AIAA Scitech 2021 Forum. https://arc.aiaa.org/doi/full/10.2514/6.2021-1260.

[19] James B. Pezent, Rohan Sood, Andrew Heaton, Kyle Miller, Les Johnson, Preliminary trajectory design for NASA's Solar Cruiser: a technology demonstration mission, Acta Astronaut. 183 (2021) 134–140, https://doi.org/10.1016/j.actaastro.2021.03.006. ISSN 0094-5765.

[20] Hörz Friedrich, et al., Impact Features on Stardust: Implications for Comet 81P/Wild 2 Dust, Science314, 2006, pp. 1716–1719, https://doi.org/10.1126/science.1135705.

[21] David Krejci, Paulo Lozano, Space propulsion technology for small spacecraft, Proc. IEEE 106 (3) (2018) 362–378.

[22] Armen Toorian, Ken Diaz, Simon Lee, The Cubesat Approach to Space Access. In 2008 IEEE Aerospace Conference, IEEE, 2008, pp. 1–14.

[23] \cite{cp1 Material}.

[24] Colin R. McInnes, Solar Sailing: Technology, Dynamics and Mission Applications, Springer Science & Business Media, 2013.

[25] Lorenzo Niccolai, Alessandro A. Quarta, Giovanni Mengali, Analytical solution of the optimal steering law for non-ideal solar sail, Aero. Sci. Technol. 62 (2017) 11–18, https://doi.org/10.1016/j.ast.2016.11.031. ISSN 1270-9638.

[26] Lorenzo Niccolai, Alessandro Anderlini, Giovanni Mengali, A. Alessandro, Quarta, Effects of optical parameter measurement uncertainties and solar irradiance fluctuations on solar sailing, Adv. Space Res. 67 (9) (2021) 2784–2794, https://doi.org/10.1016/j.asr.2019.11.037. ISSN 0273-1177.

[27] Jie Zou, Dongxu Li, Jie Wang, Yu Ye, Experimental study of measuring the wrinkle of solar sails, Aerospace 9 (6) (2022) 289, https://doi.org/10.3390/aerospace9060289.

[28] Bernd Dachwald, Malcolm Macdonald, Colin R. McInnes, Giovanni Mengali, Alessandro A. Quarta, Impact of optical degradation on solar sail mission performance, J. Spacecraft Rockets 44 (4) (2007) 740–749.

[29] Rachel S. Zoll, Craig B. Schindler, Travis L. Massey, Daniel S. Drew, Michel M. Maharbiz, Kristofer SJ. Pister, Mems-actuated carbon fiber microelectrode for neural recording, IEEE Trans. NanoBioscience 18 (2) (2019) 234–239.

[30] Daniel Teal, Hani C. Gomez, Craig B. Schindler, Kristofer S.J. Pister, Robust Electrostatic Inchworm Motors for Macroscopic Manipulation and Movement. 2021 21st International Conference on Solid-State Sensors, Actuators and Microsystems (Transducers), 2021.

[31] John E. Rogers, Phillip M. Ozmun, John Y. Hung, Robert N. Dean, Bi-directional gap closing mems actuator using timing and control techniques, in: IECON 2006-32nd Annual Conference on IEEE Industrial Electronics, IEEE, 2006, p. 3149. –3154.

[32] Carl Christian Liebe, Pattern recognition of star constellations for spacecraft applications, IEEE Aero. Electron. Syst. Mag. 8 (1) (1993) 31–39.

[33] C. Whitmell, Brightness of a planet, Observatory 30 (1907) 96–100.

[34] A.B. Chamberlin, D.K. Yeomans, Jpl small-body database browser, in: Jet Propulsion Laboratory: Solar System Dynamics, 2010. http://ssd.jpl.nasa.gov/sbdb.cgi#top.

[35] Esther Morrow, Daniel J. Scheeres, Dan Lubin, Solar sail orbit operations at asteroids, J. Spacecraft Rockets 38 (2) (2001) 279–286.

[36] Giovanni Mengali, Alessandro A. Quarta, Optimal three-dimensional interplanetary rendezvous using nonideal solar sail, J. Guid. Control Dynam. 28 (1) (2005) 173–177.

[37] B. Açıkmeşe M. Szmuk, Successive Convexification for 6-dof Mars Rocket Powered Landing with Free-Final-Time, Proceedings of the AIAA SciTech Forum, San Diego, CA, USA, January 2018.

[38] Daniel R. Wibben, Andrew Levine, Samantha Rieger, James V. McAdams, Peter G. Antreasian, Jason M. Leonard, Michael C. Moreau, Dante S. Lauretta, Osiris-rex frozen orbit design and flight experience, in: AAS/AIAA Astrodynamics Specialist Conference, 2019, Univelt Inc., 2020, pp. 2959–2971.

[39] Y.C. Ho A.E. Bryson Jr., Applied Optimal Control, Taylor & Francis, 1975.

[40] Vincent W.S. Chan, Free-space optical communications, J. Lightwave Technol. 24 (12) (Dec 2006) 4750–4762.

[41] M.W. Fishburn, Fundamentals of CMOS Single-Photon Avalanche Diodes, Delft University of Technology, 2012. PhD thesis.

[42] L. Ratti, P. Brogi, G. Collazuol, G. Dalla Betta, A. Ficorella, L. Lodola, P. S. Marrocchesi, S. Mattiazzo, F. Morsani, M. Musacci, L. Pancheri, C. Vacchi, Dark count rate degradation in cmos spads exposed to x-rays and neutrons, IEEE Trans. Nucl. Sci. 66 (2) (2019) 567–574.

[43] J.A. Richardson, L.A. Grant, R.K. Henderson, Low dark count single-photon avalanche diode structure compatible with standard nanometer scale cmos technology, IEEE Photon. Technol. Lett. 21 (14) (2009) 1020–1022.

[44] E. Sarbazi, M. Safari, H. Haas, The bit error performance and information transfer rate of spad array optical receivers, IEEE Trans. Commun. 68 (9) (2020) 5689–5705.

[45] A. Ficorella, L. Pancheri, G.D. Betta, P. Brogi, G. Collazuol, P.S. Marrocchesi, F. Morsani, L. Ratti, A. Savoy-Navarro, Crosstalk Mapping in Cmos Spad Arrays. In 2016 46th European Solid-State Device Research Conference (ESSDERC), 2016, pp. 101–104.

[46] D. Chitnis, S. Collins, A spad-based photon detecting system for optical communications, J. Lightwave Technol. 32 (10) (5 2014) 2028–2034.

[47] The Nist Stars Program – Update 2017, 2017.

[48] Matt Last, Brian S. Leibowitz, Baris Cagdaser, Jog Anand, Lixia Zhou, B. Boser, Kristofer SJ. Pister, Toward a wireless optical communication link between two small unmanned aerial vehicles, in: Proceedings of the 2003 International Symposium on Circuits and Systems, 2003. ISCAS'03, vol. 3, IEEE, 2003, p. III. III.

[49] Brian S. Leibowitz, Bernhard E. Boser, Kristofer SJ. Pister, A 256-element cmos imaging receiver for freespace optical communication, IEEE J. Solid State Circ. 40 (9) (2005) 1948–1956.

[50] VoCore Studio, Vocore2: the Coin-Sized Linux Computer, 2020.

[51] Reitz Guenther, Thomas Berger, Daniel Matthiae, Radiation exposure in the moon environment, Planet. Space Sci. 74 (1) (2012) 78–83.

[52] Ts P. Dachev, B.T. Tomov, Yu N. Matviichuk, P.S. Dimitrov, S.V. Vadawale, J. N. Goswami, G. De Angelis, V. Girish, An overview of radom results for earth and moon radiation environment on chandrayaan-1 satellite, Adv. Space Res. 48 (5) (2011) 779–791.

[53] Alankrita Isha Mrigakshi, Daniel Matthiä, Thomas Berger, Günther Reitz, Robert F. Wimmer-Schweingruber, How galactic cosmic ray models affect the estimation of radiation exposure in space, Adv. Space Res. 51 (5) (2013) 825–834.

[54] Harold Hughes, Patrick McMarr, Michael Alles, Enxia Zhang, Charles Arutt, Bruce Doris, Derrick Liu, Richard Southwick, Philip Oldiges, Total Ionizing Dose Radiation Effects on 14 Nm Finfet and Soi Utbb Technologies. In 2015 IEEE Radiation Effects Data Workshop (REDW), IEEE, 2015, pp. 1–6.

Alexander N. Alvara is a PhD candidate in the Department of Mechanical Engineering at University of California, Berkeley co-advised by Professor Liwei Lin and Professor Kristofer Pister with the Berkeley Actuators and Sensor Center. He received his three concurrent BS degrees in Mechanical Engineering, Aerospace Engineering, as well as Materials Science and Engineering at University of California, Irvine in 2017. Alexander's research is focused on micro-/nano-systems and materials with applications in extreme environments.

Lydia Lee is a PhD student in the Department of Electrical Engineering and Computer Sciences at University of California, Berkeley, advised by Professor Kristofer Pister in the Berkeley Autonomous Microsystems Lab. She received her BS in Electrical Engineering and Computer Sciences from University of California, Berkeley in 2017. Her research focuses on automated design of sensor front ends for low power electronics and space applications.

Emmanuel Sin recently finished his PhD in the Department of Mechanical Engineering at the University of California, Berkeley. He received his BS in Mechanical Engineering from Massachusetts Institute of Technology in 2007. His research interests are in aerospace guidance, navigation, and control.

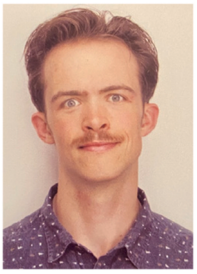

Nathan Lambert recently finished his PhD at the University of California, Berkeley. He was a member Department of Electrical Engineering and Computer Sciences, advised by Professor Kristofer Pister in the Berkeley Autonomous Microsystems Lab. His work explores many topics on model learning and decision making with data-driven and analytical methods. He received his BS in Electrical and Computer Engineering from Cornell University in 2017.

Andrew Westphal is a Research Physicist and Senior Space Fellow at the Space Sciences Laboratory at U. C. Berkeley. He got his PhD at Berkeley in 1992 in high-energy astrophysics, and now works on the interface between planetary science and astrophysics. The Westphal group uses some of the most sophisticated x-ray, electron-beam and ion-beam instruments on the planet to study ultra-primitive extraterrestrial materials that contain clues about the earliest history of the solar system.

Kristofer S. J. Pister is a professor of Electrical Engineering and Computer Sciences at University of California, Berkeley and the founder and CTO of Dust Networks. He received a BA in Applied Physics from University of California, San Diego, 1986, and an M.S. and PhD in EECS from University of California, Berkeley in 1989 and 1992. Prior to joining the faculty of EECS in 1996, he taught in the Electrical Engineering Department, University of California, Los Angeles.